

# Acoustic streaming in micromachined flexural plate wave devices: numerical simulation and experimental verification

Nam-Trung Nguyen, Richard M. White, *Fellow, IEEE*

**Abstract**— This paper presents the numerical simulation and experimental validation of acoustic streaming in micromachined flexural plate wave (FPW) devices. Two-dimensional and Three-dimensional models of two device types were considered: the classical device with parallel interdigitated electrodes and the focused device with curved electrodes. Influences of different parameters on the time-average velocity were investigated. Thermal transport effects of the acoustic streaming were also considered. We observed the amplifying effect of the streaming in the second type numerically and experimentally. In order to verify simulation results, the method of the Particle Image Velocimetry (PIV) was applied in the experimental investigation.

**Keywords**— flexural plate waves, microfluidics, acoustic streaming, computational fluid mechanics, and particle image velocimetry

## I. INTRODUCTION

IN the last years, a new research field called microfluidics has been established. This field focused on the application of micromachined devices for handling small amount of fluids like pumping, mixing, and sensing fluids as well as components carried by those fluids. Such devices have different applications in microbiology and microchemical analysis, where different fluids on nanoliter to microliter ranges can be controlled and delivered [1], [2], [3].

The acoustic streaming is a well-known effect, in which an acoustic field causes a net fluid flow. Ref. [4] gives a comprehensive analytical investigation of this effect. Many recent publications have shown interest in the use of the acoustic streaming in the flexural plate wave (FPW) devices for fluid pumping [5], [6]. For designing micropumps with this principle, it is important to understand the relation between the pumping behaviour and the design parameters. A complex numerical simulation will be necessary.

When a flexural wave propagates in a thin membrane, an acoustic field appears in the fluid near the surface. This acoustic field causes fluid flows in the wave direction. The micromachined device consists of a rectangular flow channel that has a thin membrane on the bottom. The membrane is made of low-stress silicon nitride, piezoelectric zinc

oxide, and aluminum. The typical thickness of the membrane is from 1 to 3 microns. The flexural plate waves have a typical frequency of 3 MHz and a wavelength of 100 microns. Interdigitated transducers (IDTs), arrays of finger pairs placed at wavelength intervals, generate the flexural waves. The focused device uses curved electrodes in order to concentrate the acoustic energy, and consequently amplify the wave amplitude as well as the flow velocity. Fig. 1 illustrates the two FPW-device types that are investigated in this paper.

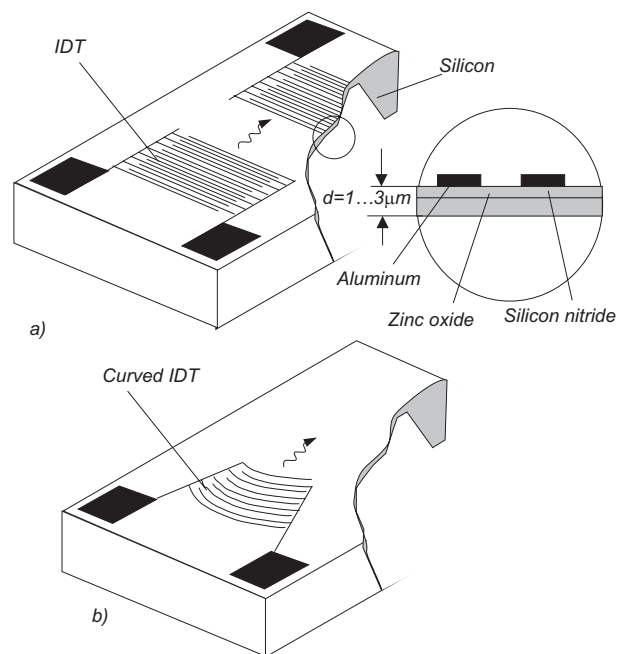


Fig. 1. Micromachined flexural plate wave devices. (a) Classical device with parallel IDTs, (b) Focused device with curved IDTs.

All published works with the FPW-devices are limited in analytical models and velocity measurement through manual optical observation [5], [7]. However, models of the focused devices and of the coupling between acoustic streaming and thermal transport are too complicated for an analytical solution. This paper presents the numerical simulation of complex thermal-coupled models of both device types. The measurement of velocity utilizes the particle image velocimetry method (PIV-method), which traces and evaluates the flow with small particles. A CCD-camera and a VCR record and provide particle images to a PC. The velocity field can be then calculated by using displacement

This work was sponsored by the Wright Laboratory, WL/POOS, Air Force Material Command, USAF, under grant number F33615-97-1-2705

Nam-Trung Nguyen is with the Berkeley Sensor & Actuator Center, Department of Electrical Engineering and Computer Sciences, University of California Berkeley, CA 94720 USA (e-mail:ntn@bsac.eecs.berkeley.edu).

Richard M. White is director of the Berkeley Sensor & Actuator Center and a professor of the Department of Electrical Engineering and Computer Sciences, University of California Berkeley, CA 94720 USA

information of particles in the captured images. Results of the numerical simulation and the experimental investigation are discussed at the end of the paper.

## II. MODEL DESCRIPTION

The numerical simulation uses a commercial computational fluid dynamics software package (CFD Research Corporation). The CFD code solves the continuity equation, the momentum equation, and the energy equation. The software permits the user to modify the fluid density using the ideal gas law or a second-order function of pressure. Therefore, it is possible to simulate the incompressible flow. Further more, temperature dependency of fluid properties can be considered, results presented here will neglect the temperature dependency.

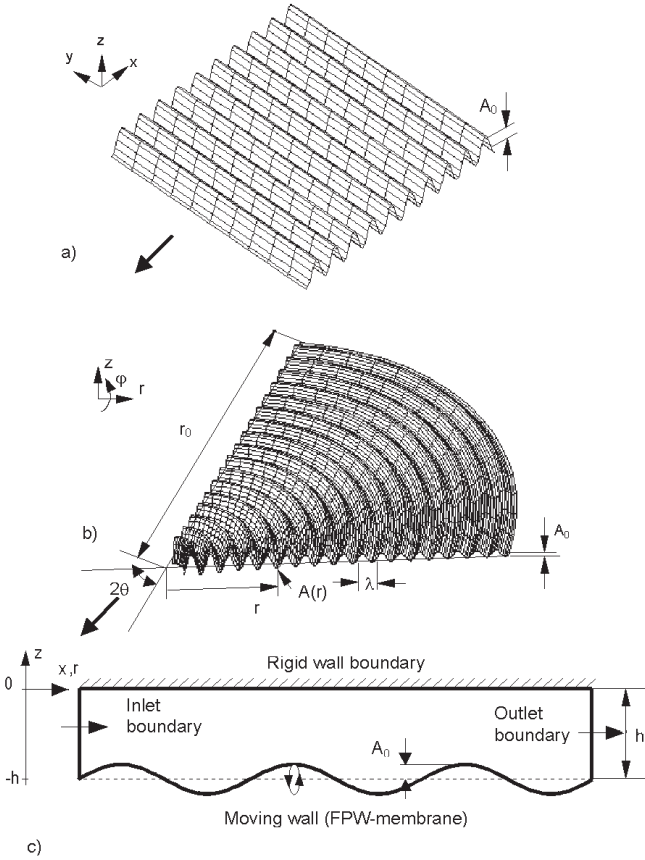


Fig. 2. Models of the FPW-device. (a) membrane surface of the classical type. (b) membrane surface of the focused type. (c) Two-dimensional model for the  $xz$ -plane

Fig. 2 describes the three-dimensional model of the membrane of the classical FPW-pump (a) and the focused FPW-pump (b). The two-dimensional model shown in Fig. 2c describes the boundary conditions in  $xz$ -plane. A user library routine written in FORTRAN modifies the grid positions in each calculated time step. We assume that the grid displacements  $\Delta x(z)$ ,  $\Delta y(z)$ , and  $\Delta z(z)$  decrease linearly from the maximum value at the driven membrane to zero at the opposite rigid wall:

$$\begin{aligned}\Delta x(z) &= \frac{\Delta x_0 \cdot z}{-h}, \\ \Delta y(z) &= \frac{\Delta y_0 \cdot z}{-h}, \\ \Delta z(z) &= \frac{\Delta z_0 \cdot z}{-h},\end{aligned}\quad (1)$$

where  $h$  is the channel height,  $\Delta x_0$ ,  $\Delta y_0$ , and  $\Delta z_0$  are the grid displacements at the driven flexural membrane which can be calculated by following models.

Fig. 2c shows how points on the device surface move elliptically in a counterclockwise direction as the flexural wave travels from left to right. The ratio of the minor to the major axis of the ellipse is given with the membrane thickness  $d$  and the wave length  $\lambda$  by  $\pi d/\lambda$  [8]. For our case, with the wavelength of  $\lambda = 100\mu\text{m}$  and the membrane thickness of  $d = 3\mu\text{m}$ , the ratio of the minor to major axis of the elliptical motion will be 0.093. At the flexural membrane, the vertical displacement  $\Delta z_0$ , the horizontal displacement  $\Delta x_0$  (classical type), and the radial displacement  $\Delta r_0$  (focused type) are given

- for the classical type:

$$\Delta z_0 = A(t) \sin(\omega t - kx), \quad (2)$$

$$\Delta x_0 = A(t) \frac{\pi d}{\lambda} \cos(\omega t - kx), \quad (3)$$

- and for the focused type:

$$\Delta z_0 = A(r, t) \sin(\omega t - kr), \quad (4)$$

$$\Delta r_0 = A(r, t) \frac{\pi d}{\lambda} \cos(\omega t - kr), \quad (5)$$

where  $A$  is the wave amplitude,  $\omega = 2\pi f$  is the angular frequency of the wave,  $k = 2\pi/\lambda$  is the wave number. The axes  $x$ ,  $r$  and  $z$  are defined in Fig. 2. The models neglect the displacement in  $y$ -axis  $\Delta y = 0$  of the classical device and the peripheral displacement  $\Delta \varphi = 0$  of the focused device. The wave amplitude is given by:

$$A = \frac{1}{\omega} \sqrt{\frac{2P_{avg}}{M_\rho w v_p}}. \quad (6)$$

where  $P_{avg}$  is the time-averaged acoustic power flowing in the wave,  $M_\rho$  is the mass density of the plate,  $w$  is the width of the acoustic beam,  $v_p$  is the phase velocity of the FPW, and  $v_s$  is the speed of sound in the fluid [5]. For the classical device with a constant plate width, the wave amplitude is assumed to be constant along the  $x$ -axis. Since acoustic beam width of the focused device is proportional to the radius:

$$w = 2\theta \cdot r, \quad (7)$$

where  $\theta$  is the convergence angle, the wave amplitude can be described as function of the radius as following:

$$A(r) = A_0 \sqrt{\frac{r_0}{r}}, \quad (8)$$

with the starting wave amplitude  $A_0$  at the starting radius  $r_0$ . Fig. 3 compares the model of Eq. (8) with the results of the laser diffraction measurement [9]. In order to make a realistic initial condition, the wave amplitude can also be described as a function of the time  $t$  for the classical type:

$$A(t) = A_0(1 - \exp \frac{-t}{\tau}), \quad (9)$$

and as a function of the time  $t$  and the radius  $r$  for the focused type:

$$A(r, t) = A_0 \sqrt{\frac{r_0}{r}} (1 - \exp \frac{-t}{\tau}). \quad (10)$$

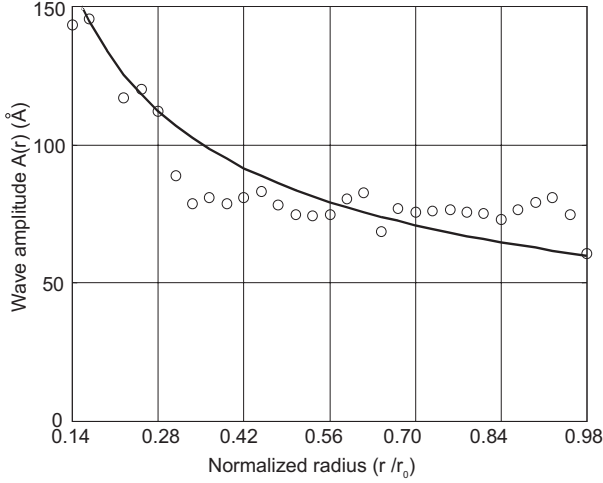


Fig. 3. Flexural wave amplitude along the normalized radius. The solid line is theoretical model from Eq. (8), the circles are results of laser diffraction measurement

The results presented in this paper use a time constant for water of one wave period  $\tau = T = 1/f$ . The stable solution establishes after 15 periods. The time-averaged velocity field can then be calculated using the results of the first-order velocity over one period.

### III. SIMULATION RESULTS

#### A. Classical device

In order to investigate the classical device, the dependence of velocity profile and flow rate on the wave amplitude, on the channel height, and on the backpressure gradient are considered. Since the displacement in y-axis can be neglected with parallel IDTs, the analysis only needs the two-dimensional model shown in Fig. 2c. The channel model has a length of three wavelengths ( $300\mu m$ ). The model contains a moving wall as the flexural surface, a rigid wall as the opposite surface, inlet, and outlet boundaries. If we assume that the channel is infinitely long compared to the wave length, the model can utilize the cyclic boundary condition which forces all variables (e. g., velocity, pressure) at the inlet and outlet to be equal. In the cases of applying a backpressure and of modeling the thermal transport, constant pressure boundaries are used for the inlet and the outlet.

With the known time-averaged velocity profile, the volume flow rate through the channel  $\dot{Q}$  can be then calculated with an integral of velocity  $u(z)$  over the channel height axis  $z$ :

$$\dot{Q} = w \cdot \int_0^h u(z) dz \quad (11)$$

where  $w$  is the channel width and  $h$  is the channel height. Because of the two-dimensional model, the channel width of the model is assumed to be  $w = 1m$ .

#### A.1 Influence of wave amplitude

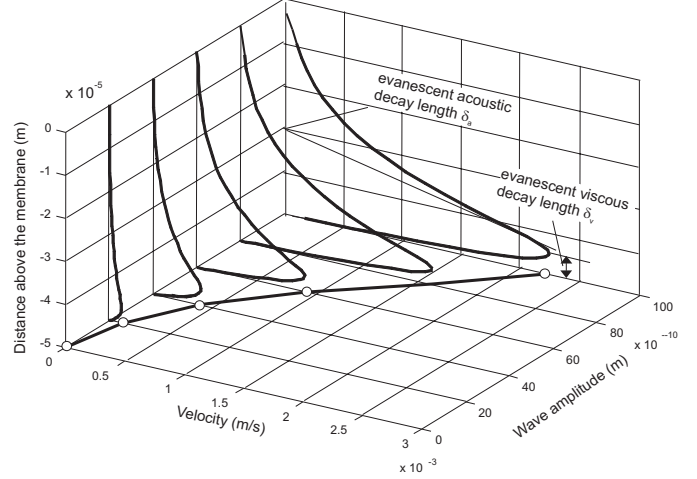


Fig. 4. Velocity profile over the channel height of 50 microns driven by different wave amplitudes (for water).

Fig.4 depicts the velocity profile as function of channel height and wave amplitude. It can be seen that the amplitude of the evanescent disturbance in the fluid adjacent to the membrane agrees with the analytical assumption:

$$v = v_{max} \exp \frac{-z}{\delta_a}, \quad (12)$$

where

$$\delta_a = \frac{\lambda}{2\pi \sqrt{1 - (v_p/v_s)^2}} \approx \frac{\lambda}{2\pi}, \quad (13)$$

$v_p$  is the phase velocity [5]. The evanescent viscous decay length  $\delta_v$  is smaller and is as shown in Fig. 4 about 5 microns.

The curve at the bottom represents the parabolic characteristic of the maximum velocity. Increasing the wave amplitude enlarges the time-averaged velocity over the whole channel. This leads to the same parabolic characteristics of the volume flow rate (Fig. 5). These non-linear characteristics were observed experimentally by Moroney et al. [5]. The results here give an unequivocal behavior of the acoustic streaming: the flow rate varies as square of driving voltage, which is proportional to the wave amplitude. Therefore, the wave amplitude and consequently the driving voltage are the most important parameters for controlling the flow rate of the acoustic streaming.

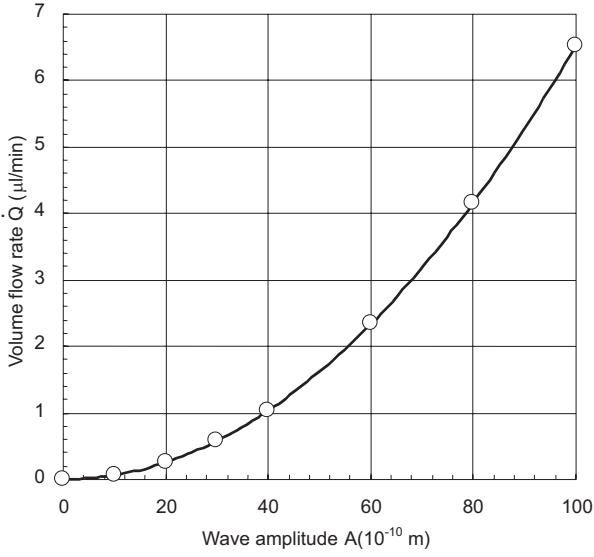


Fig. 5. Volume flow rates versus wave amplitude (3mm x 50 microns channel). The circles are simulated results, and the solid line is the second-order polynomial fitting function.

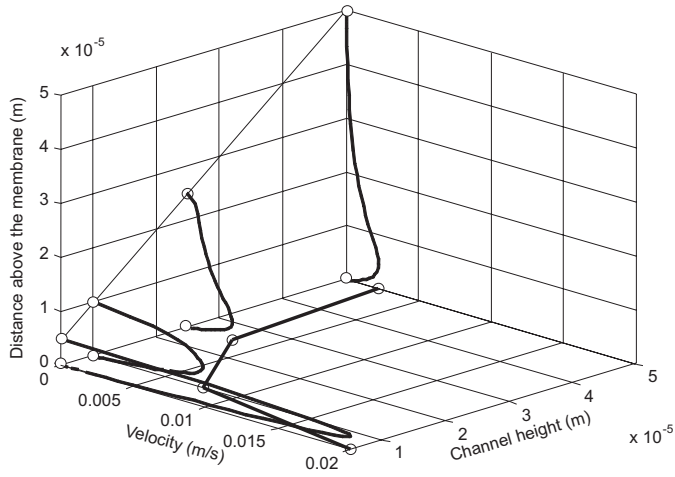


Fig. 6. Velocity profile with different channel heights driven by an wave amplitude of 0.1nm(for water).

## A.2 Influence of channel height

The velocity profiles in a channel with different heights and the wave amplitude of 0.1nm are shown in Fig. 6. The curve at the bottom represents the maximum velocity of each profile. This curve shows clearly that the maximum velocity stays constant with a channel height that is greater than the evanescent decay length of the acoustic wave in the fluid. The particle velocities in the channel beyond the evanescent decay distance are small. The maximum velocity is constant (Fig. 6). Therefore, the volume flow rates of a channel with heights greater than twice of decay length are invariable at constant driving wave amplitude. That can be proved in Fig. 7, which shows the volume flow rate versus the channel height.

The results show that optimizing the channel height only

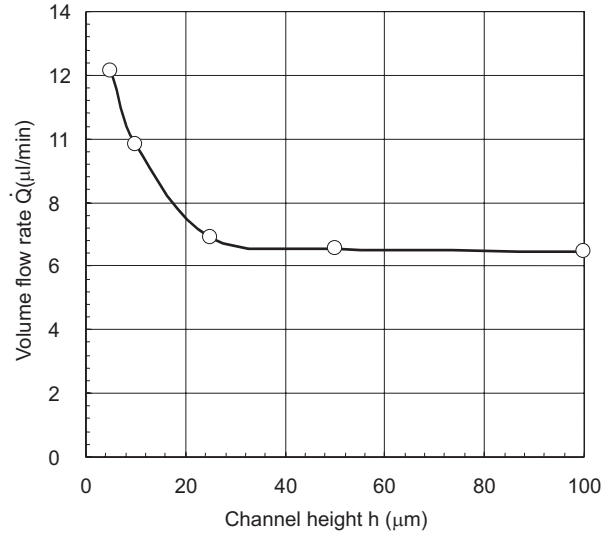


Fig. 7. Volume flow rates versus channel heights (3mm channel width, 10nm wave amplitude). The circles are simulated results, and the solid curve is non-linear fitting function.

makes sense with values less than the evanescent decay length of the acoustic wave (about 20 microns). In this small channel, the time-averaged velocity has a typical parabolic profile and high values (Fig. 6). However, decreasing the channel height does not change the flow rate so fast as the maximum velocity because the flow rate is proportional to the maximum velocity and the channel height respectively. A five micron high channel has about ten times the maximum velocity (Fig. 6) but only about two times volume flow rate compared to one whose height is 50 microns (Fig. 7).

## A.3 Influence of the backpressure

The performance of acoustic streaming can be investigated by applying a backpressure against the flow direction (wave propagation direction). If a backpressure pushes against the acoustically induced flow, the flow in the channel is a combination of viscous and acoustic streaming (Fig. 8). The backward flow (viscous) increases during forward flow (acoustic) decreases proportionally to the applied backpressure. This flow phenomenon was observed experimentally by Luginbuhl *et al.* [6].

## A.4 Thermal transfer caused by acoustic streaming

If the acoustic streaming induces a net mass transfer as described above, it also causes a thermal transfer. In the model, a limited section of the wall (100 microns) is heated with a constant heating power. Heat conduction in the nitride membrane is neglected. Since the time response of the thermal system in the FPW-device lies in a range of few milliseconds, the thermal response (less than 1 KHz) is much slower than the change of the time-dependent velocity (3 MHz). The huge difference between the time period of the acoustic wave and the thermal response time also causes a technical problem for the simulation. The calculation time after Eq. 9 or Eq. 10 is too fast compared to the

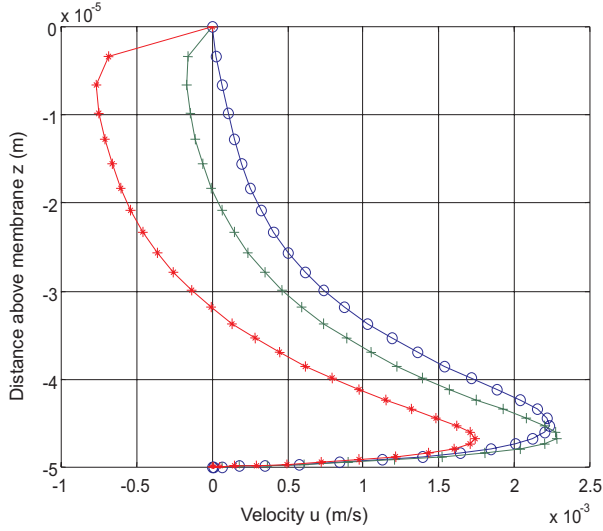


Fig. 8. Velocity profile of 50-micron channel with different back-pressures (o:  $0\text{ Pa}$ ; +:  $0.5 \times 10^5\text{ Pa/m}$ ; \*:  $1.74 \times 10^5\text{ Pa/m}$ , for water)

thermal response of the model. Therefore, a static thermal analysis for the model without acoustic streaming should be done first. Then the resulting temperature field (see Fig. 10a) can be used as initial condition for the actual thermal-coupled simulation.

The acoustic streaming causes a very weak thermal transfer effect because of the small time-averaged fluid flow rate. Significant cooling effects can only be observed with the large wave amplitude of  $100\text{ nm}$ . Because of the heat transfer to the opposite wall, the forced convection of acoustic streaming is more effective than that produced by Poiseuille-flow for the same net flow rate. Fig. 9 compares the convective heat loss:

$$P_{conv.}(\dot{Q}) = P(\dot{Q}) - P(0) \quad (14)$$

for these two flow types. The heat loss of acoustic streaming in the low flow rate range is about 100 times larger than that of Poiseuille-flow because the heat transfer to the opposite wall dominates the forced convection in the streaming direction.

Fig. 10b shows the final result of the thermal-coupled simulation in a three-dimensional model for a closed classical FPW-device. The result shows clearly the displacement in wave propagation direction of the temperature profile near the membrane surface. Since the etched well is closed, the flow turns around on the top of the channel and also causes a thermal displacement in the opposite direction. Bradley *et al.* also observed the turn-around flow experimentally with particle tracing method [7].

### B. Focused device

Since formulating the focused FPW-device (Fig. 2b) needs a polar coordinate system, the simulation only works with a three-dimensional model. The grid displacement at the membrane in x-axis and y-axis can be calculated by

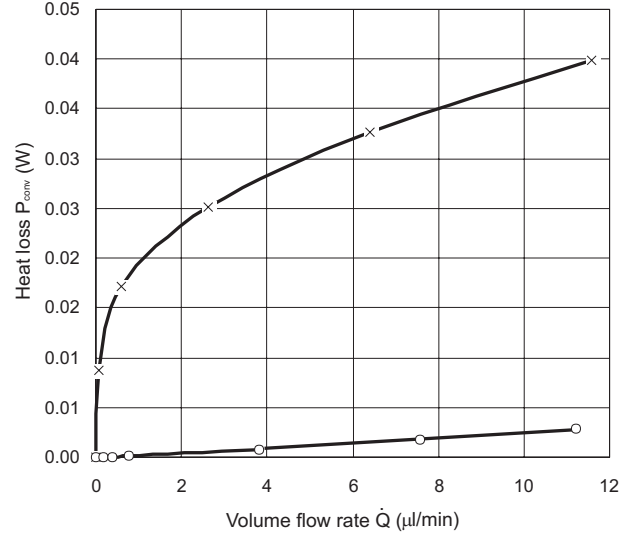


Fig. 9. Heat loss caused by forced convection of acoustic streaming (x) and Poiseuille-flow (o) (channel with  $3\text{ mm}$  width,  $5\text{ }\mu\text{m}$  height,  $100\text{ }\mu\text{m}$  heater length, the conductive loss without streaming is  $P(0) = 0.9\text{ W}$ , for water).

the position coordinates  $(x, y)$  and the radial displacement  $\Delta r_0$  given in Eq. (5):

$$\begin{aligned} \Delta x_0 &= \frac{\Delta r_0 x}{r} = \frac{\Delta r_0 x}{\sqrt{x^2 + y^2}} \\ \Delta y_0 &= \frac{\Delta r_0 y}{r} = \frac{\Delta r_0 y}{\sqrt{x^2 + y^2}}. \end{aligned} \quad (15)$$

After the model of Eq. (8), the wave amplitude would go to infinity  $A \rightarrow \infty$  if the radius goes to zero  $r \rightarrow 0$ . Therefore, the r-axis (see Fig. 2) is chosen in the range  $100\text{ }\mu\text{m} \leq r \leq r_0$ . The resulting velocity profiles in z-axis are similar to those of the classical devices (see Fig. 4 and Fig. 6). Fig. 11 illustrates the field of maximum velocities in x-y-plane which shows clearly the amplifying effect caused by focusing the flow and by increasing the wave amplitude (see Eq. 8 and Fig. 3).

## IV. EXPERIMENTAL VERIFICATION

For comparison with the measurement, results of Moroney *et al.* [5] are taken. The velocities along the membrane surface are measured with a closed FPW-device. A cover slip acts as a cap on the well to reduce vaporization. Polystyrene particles with  $2.3\text{ }\mu\text{m}$ -diameter and a specific gravity of 1.05 were used for tracing the flow. The presented results are flow velocities evaluated at  $2\text{ }\mu\text{m}$  above the membrane. Because of the high velocity gradient near the surface and the complicated interaction between flowing fluid and solid particles, the velocity of the particles should be smaller than the velocity at  $2\text{ }\mu\text{m}$  above the membrane. The simulated results here are corrected by a factor  $K$  in order to fit the experimental results:

$$v_{corrected} = K \cdot v_{simulated}. \quad (16)$$

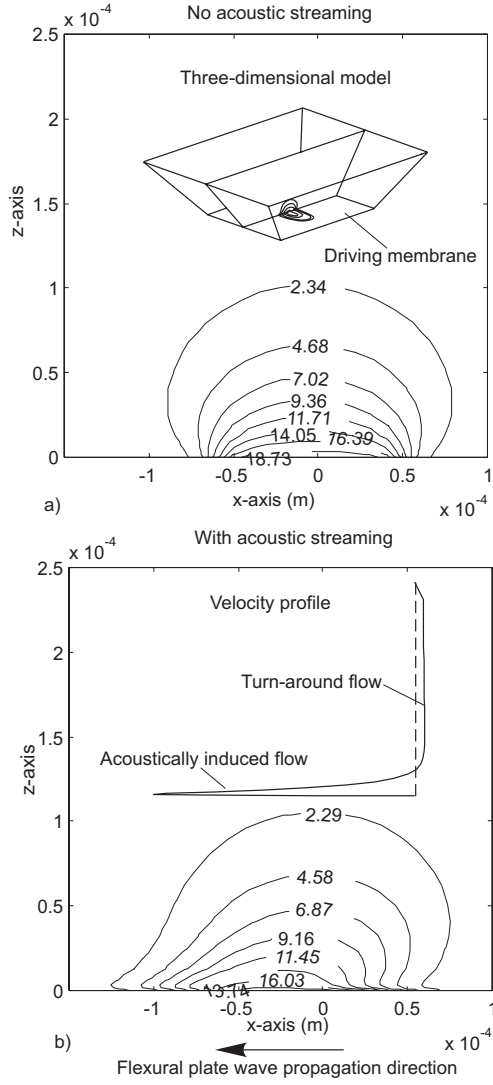


Fig. 10. Temperature profile in a closed FPW-device: (a) no acoustic streaming, (b) with acoustic streaming. The displacement of the temperature distribution indicates the acoustic streaming and the turn-around flow (b) (The wave amplitude is  $0.1 \mu\text{m}$ , constant heat flux  $Q = 8 \cdot 10^5 \text{ W m}^{-2}$ , for water).

Thus results presented in Fig. 12 should be seen as a qualitative comparison.

The particle image velocimetry (PIV) analysis is based on the particle displacement analysis of two snapshots of flow images traced with small particles. The principle can be simply explained by the following equation:

$$v = \alpha \frac{s}{\Delta t}, \quad (17)$$

where  $s$  (in pixels) is the particle displacement,  $\Delta t$  (in seconds) is the time difference between the two frames,  $\alpha$  (m/pixel) is the space ratio that convert pixels to the real geometry and  $v$  (in m/s) is the velocity of the particle.

Since the beginning of the nineties the correlation algorithm plays an important role for the evaluation of PIV-images. Two images of the particle-laden flow are captured, either in one image or in two. After recording the images,

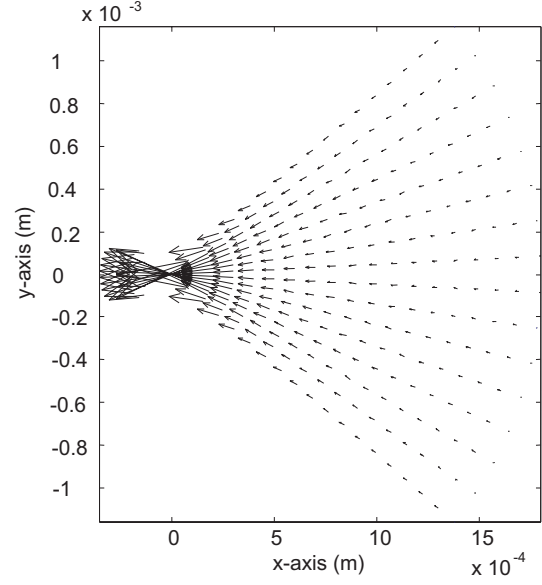


Fig. 11. Maximum velocity field of the focused FPW-device in x-y-plane ( $r_0 = 1700 \mu\text{m}$ ,  $\theta = 40^\circ$ )

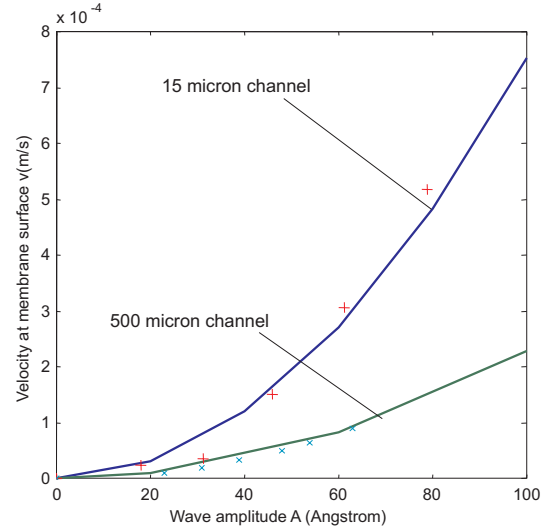


Fig. 12. Measured flow velocity at the membrane surface (+ and x) and corrected simulation results (solid line) for 15 micron and 500 micron channels

the image plane is divided into a grid of rectangular interrogation windows. For each interrogation window of  $M \times N$  pixels, the velocity of the middle point of the window can be calculated using the cross-correlation of the interrogation regions [10].

With the gray value function  $g_1(i, j)$  and  $g_2(i, j)$  of the two pictures, the cross-correlation  $\Phi(m, n)$  can be describes as:

$$\Phi(m, n) = \sum_{i=1}^M \sum_{j=1}^N g_1(i, j) g_2(i + m, j + n). \quad (18)$$

Using the two-dimensional Fast-Fourier-Transformation (FFT), this algorithm can be carried out fast and simply

as following:

- calculation of FFT functions  $\hat{g}_1$  and  $\hat{g}_2$  of each interrogation window,
- calculation of the conjugated FFT function  $\hat{g}_2^*$  of the second window,
- calculation of the complex product  $\Phi = \hat{g}_1 \cdot \hat{g}_2^*$ , and
- calculation of the invert two-dimensional FFT.

The maximum value of  $\Phi$  (peak) indicates where the two images are most similar, which represents the mean displacement of the particles in each interrogation window between the two snapshots. If the particle snapshots are recorded on a single image, each interrogation window should be auto-correlated. The algorithm of the auto-correlation is similar as that of the cross-correlation described above.

To improve the resolution and accuracy the PIV-analysis requires an algorithm capable of tracking displacements to sub-pixel accuracy. Assuming the cross-correlation  $\Phi(\xi)$  is a Gaussian distribution function with the standard deviation  $\sigma$ :

$$\Phi(\xi) = \frac{1}{\sigma\sqrt{2\pi}} \exp\left[-\frac{(\xi - \xi_0)^2}{2\sigma^2}\right], \quad (19)$$

the sub-pixel estimator is:

$$\xi_0 = \frac{(\xi_2^2 - \xi_1^2)\ln(\Phi_2/\Phi_3) - (\xi_2^3 - \xi_2^2)\ln(\Phi_1/\Phi_2)}{2[(\xi_2 - \xi_1)\ln(\Phi_2/\Phi_3) - (\xi_3 - \xi_2)\ln(\Phi_1/\Phi_2)]}, \quad (20)$$

where  $\xi_0$  denotes the estimated displacement,  $\xi_1, \xi_2, \xi_3$  are the locations of the left of peak, peak, and right of peak intensity.  $\Phi_1, \Phi_2, \Phi_3$  are the cross-correlation value at  $\xi_1, \xi_2, \xi_3$  [11].

Noise in the particle image and stochastic influence of Brownian motion can be eliminated by averaging the results of more image pairs [12]. The measurement of the velocity field is carried out with a microscope, a CCD-camera, and a video recorder. Frame images are then captured and transferred to the PC and analyzed there. The relative error due to Brownian motion is given by [12]:

$$\varepsilon = \frac{1}{v} \sqrt{\frac{2\kappa_B T}{3\pi\mu d_p \Delta t}} \quad (21)$$

where  $v$  is the characteristic velocity,  $\kappa_B = 1.28e - 23(J/K)$  is the Boltzman's constant,  $T$  is the absolute temperature,  $\mu$  is the dynamic viscosity of the fluid,  $d_p$  is the particle diameter, and  $\Delta t$  is the time between two snapshots. With a characteristic velocity of  $100\mu m/s$ , a particle diameter of  $2.3\mu m$ , a time between two snapshots of  $30ms$ , and the fluid temperature of  $300K$ , the error due to Brownian motion in our experiment will be 4%. Fig. 14 illustrates the velocity field in the measured area of the focused FPW-device shown in Fig. 13. The images are made with  $2.3\mu m$  fluoresced polystyrene particles in water. The analysis uses a commercial PIV-program (VidPIV, Optical Flow System, UK) or routines written in MATLAB which utilize the algorithm described above. Fig. 15 shows clearly the amplifying effect, which agrees well with simulation results.

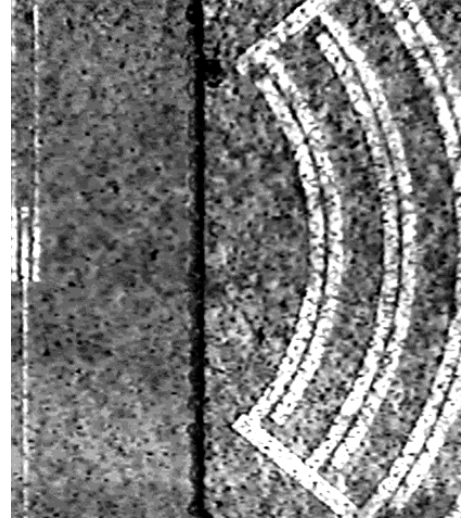


Fig. 13. Original image of the focused FPW-device for PIV-analysis

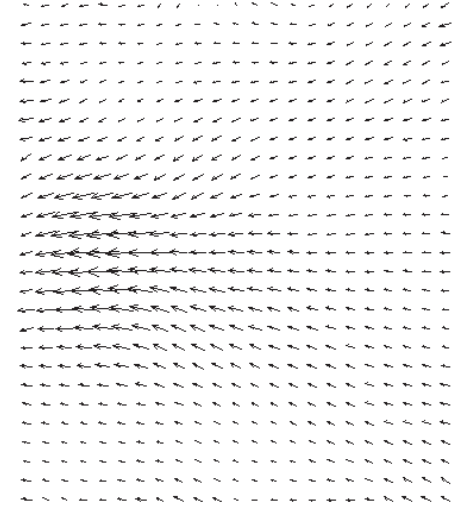


Fig. 14. Result of PIV-analysis: velocity field in the focused FPW-device shown in Fig. 14 (Grid space:  $16pixels$ ; interrogation size:  $32 \times 32pixels^2$ ).

## V. CONCLUSIONS

This paper presents new results of the numerical simulation and the experimental investigation of acoustic streaming in micromachined FPW-devices. Three-dimensional and two-dimensional models are simulated using commercial CFD software. The resulting velocity fields of the acoustic streaming agree qualitatively with the measurement. The particle image velocimetry has shown its capability for investigating acoustically induced flow.

Simulation results of the classical device confirm the possibility of using the FPW-device as a micropump. This pumping principle is gentle and suitable for biomedical and biochemical analysis. The results on the dependencies of volume flow rates on different parameters make the design of those micromachined FPW-pump easier. The most important design parameters are the channel height and the



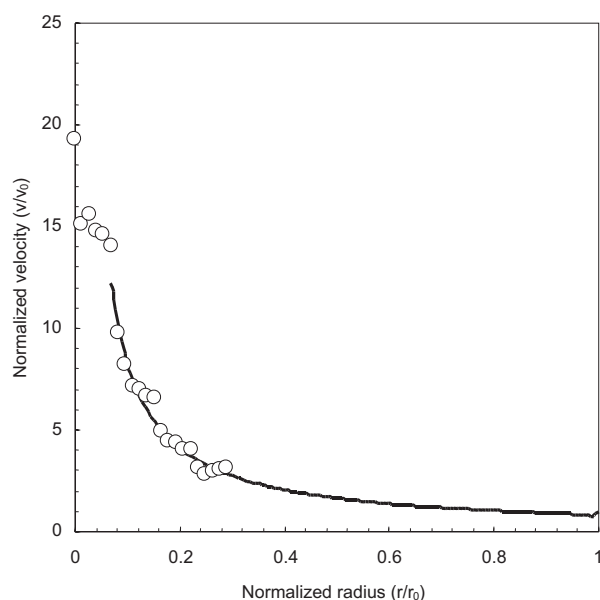


Fig. 15. Qualitative comparison between numerical simulation and PIV-measurement of the velocity profile along the radius  $r$ . Solid line is the normalized simulation results, circles are normalized measurement points

wave amplitude.

Coupled thermal analysis show the possibility of active cooling using acoustic streaming. Since the acoustically induced flow modulates the temperature profile can be by , it is possible to integrate a thermal flow sensor into a FPW-device. Thus a complete microfluidic system with pump and flow sensor in a single chip can be simply designed and fabricated.

Results of PIV-analysis has shown that this method is suitable for investigating microfluidic systems in general and for characterization of acoustic streaming in micro-machined FPW-devices in particular. However in order to improve the analysis quality, work should be done on optimization of particle size, on particle density in measured fluid, and on interaction between acoustic streaming and tracing particle. The measured velocities presented in this paper are smaller than the simulated values, finding a correction factor as function of different parameters like particle size, particle density would be an interesting future work.

#### ACKNOWLEDGMENTS

The authors would like to thank Dr. Amit Lal and the staff of CFDRC Research Corporation for the initial work. We also thank Audra Meng for results of the laser diffraction measurement as well as the PIV-experiment setup.

Effort sponsored by the Wright Laboratory, WL/POOS, Air Force Material Command, USAF, under grant number F33615-97-1-2705. The U.S. Government is authorized to reproduce and distribute reprints for governmental purposes notwithstanding any copyright notation thereon. The view and conclusions contained herein are those of the authors and should not be interpreted as necessarily rep-

resenting the official policies or endorsements, either expressed or implied, of the Wright Laboratory, WL/POOS or the U.S. Government.

#### REFERENCES

- [1] S. Shoji, M. Esashi, *Microflow Devices and Systems*, J. Micromech. Microeng. 4, 1994, pp. 157-171.
- [2] P. Gravesen, J. Branebjerg, O. S. Jensen, *Microfluidics -a Review*, J. Micromech. Microeng. 3, 1993, pp. 168-182.
- [3] M. Elwenspoek, T.S. Lammerink, R. Miyake and J. H. J. Fluitman, *Towards Integrated Microliquid Handling Systems*, J. Micromech. Microeng. 4, 1994, pp. 227-245.
- [4] W. L. Nyborg, *Acoustic streaming*, Physical Acoustics, Ed. W. P. Mason, Vol. 2B, Academic Press, 1965, pp. 265-330.
- [5] R. M. Moroney, R. M. White, R. T. Howe, *Microtransport induced by ultrasonic Lamb waves*, Applied Physics Letters, 59,7(1991), pp. 774-776.
- [6] P. Luginbuhl, S. D. Collins, G. A. Racine, M. A. Gre'tillat, N. F. de Rooij, K. G. Brooks and N. Setter, *Microfabricated Lamb wave device based on PZT sol-gel thin film for mechanical transport of solid particles and liquids*, Journal of Microelectromechanical Systems, 6, 4(1997), pp. 337-346.
- [7] C. E. Bradley, R. M. White *Acoustically driven flow in flexural plate wave devices: Theory and experiments*, Proc. IEEE Ultrasonics Symp. (1994), pp. 593-597.
- [8] T. Sashida and T. Kenjo *An Introduction to Ultrasonic Motors*, Oxford: Clarendon Press, 1993, pp. 130.
- [9] A. Meng, N. T. Nguyen, R. M. White *Focused FPW-devices*, unpublished.
- [10] R. J. Adrian *Particle-imaging techniques for experimental fluid mechanics*, Annu. Rev. Fluid Mech. 23, 1991, pp. 261-304.
- [11] E. A. Cowen, S. G. Monismith *A hybrid digital particle tracking velocimetry technique*, Experiments in Fluids 22, 1997, pp. 199-211.
- [12] J. G. Santiago, S. T. Wereley, C. D. Meinhart, D. J. Beebe, R. J. Adrian *A particle image velocimetry system for microfluidics*, Experiments in Fluids, 1998, in press.

**Nam-Trung Nguyen** was born in Hanoi, Vietnam, in 1970. He received the Dipl.-Ing. and the Dr. -Ing. Degree in Electronic Engineering from the Chemnitz University of Technology, Germany, in 1993 and 1997 respectively. In Germany, his research was focused on microfluidic devices: micropumps, microvalves and flow sensors. In 1996 he visited the University of Twente, MESA Research Institute (Netherlands) and worked with the MICMEC-group on simulation of micromachined thermal flow sensors. Since January 1998, he has been working as a postdoctoral research engineer in the Berkeley Sensor and Actuator Center (EECS, University of California Berkeley), where he is involved with research on microfluidic systems based on FPW-devices.

**Richard M. White** is a professor in the electrical engineering and computer sciences department at the University of California, Berkeley. After obtaining his bachelor's, master's and doctor of philosophy degree in engineering science and applied physics at Harvard, he worked for 6 years on microwave devices at the General Electric Microwave Laboratory in Palo Alto. He has taught and carried out research chiefly in solid-state sensors, as well as individualized instruction and the appropriate use of instructional technology. He is an IEEE Fellow and a director of Berkeley Sensor and Actuator Center.